Energy-based descriptors for photo-catalytically active metal-organic framework discovery

Fumanal, Maria; Capano, Gloria; Barthel, Senja; Smit, Berend; Tavernelli, Ivano

published in
Journal of Materials Chemistry A
2020

DOI (link to publisher)
10.1039/C9TA13506E

document version
Publisher's PDF, also known as Version of record

Journal of Materials Chemistry A

ROYAL SOCIETY OF CHEMISTRY

PAPER

View Article Online
View Journal | View Issue

Cite this: *J. Mater. Chem. A*, 2020, **8**, 4473

Energy-based descriptors for photo-catalytically active metal–organic framework discovery†

Maria Fumanal, *[ab] Gloria Capano,[a] Senja Barthel, [ac] Berend Smit [a] and Ivano Tavernelli*[b]

Received 10th December 2019
Accepted 5th February 2020

DOI: 10.1039/c9ta13506e

rsc.li/materials-a

Metal–organic frameworks (MOFs) consist of metal nodes that are connected by organic linkers. They are thus highly chemically tunable materials given the broad range of potential linkers and nodes that can be chosen for their synthesis. Their tunability has recently sparked interest in the development of new MOF photo-catalysts for energy-related applications such as hydrogen (H_2) evolution and CO_2 reduction. The sheer number of potentially synthesizable MOFs requires defining descriptors that allow prediction of their performance with this aim. Herein we propose a systematic computational protocol to determine two energy-based descriptors that are directly related to the performance of a MOF as a photocatalyst. These descriptors assess the UV-vis light absorption capability and the band energy alignment with respect to redox processes and/or co-catalyst energy levels. High-throughput screening based on cost-effective computations of these features is envisioned to aid the discovery of new promising photoactive systems.

Introduction

Metal–organic frameworks (MOFs)[1] are crystalline materials consisting in metal clusters that are connected by organic linkers and are potentially porous. They are of interest for many applications due to their often highly accessible surface areas. Among porous materials, MOFs have been shown to be promising materials for several applications such as gas storage,[2] gas separation,[3] catalysis[4,5] and sensing,[6] due to their structural tunability, adjustable topology framework and chemical functionality.[7–9] These characteristics have recently been used for the development of efficient photocatalysts in order to address solar-driven chemical reactions such as hydrogen (H_2) evolution and CO_2 reduction.[10–14] The usage of MOFs for photocatalysis may overcome the main drawbacks of traditional TiO_2 and CdS photocatalysts. For example, TiO_2 has poor visible light absorption, while CdS has poor photostability. Using MOFs we might be able to design materials with improved photocatalytic performance by means of strategic selection of light-responsive ligands and reductive metal ions such as Ti(IV) and Zr(IV).[15] For instance, remarkable H_2 production has been reported for different photocatalytic systems based on visible-light active MOFs such as MIL-125-NH_2 (ref. 10 and 11) or the recently reported ZSTU-family.[16]

The modular nature of MOFs causes an almost unlimited number of hypothetical structures, which makes the traditional trial and error strategies to find materials of interest unfeasible. This explains the popularity of computational screening of MOFs to tentatively predict target properties and to guide future efforts in synthesis. Previous high-throughput screening studies of MOFs were developed to characterize their geometrical features, such as the pore size distribution and accessible surface area, while Grand Canonical Monte Carlo (GCMC) and Molecular Dynamics (MD) simulations were used to compute and screen their target gas adsorption performance.[17–22] More recently, a high-throughput scheme for heterogeneous catalysis screening of MOFs was reported.[23] These and other studies rely on the generation of large databases of MOFs, experimental or hypothetical. These efforts have produced a vast library of MOFs for which photo-catalytic activity has not been tested, and neither has their potential been evaluated. Screening the databases for the photo-catalytic activity will identify materials that are promising photocatalysts.

A typical scheme of a photo-catalytic system with MOFs includes a co-catalyst and a sacrificial agent as depicted in Fig. 1. The photo-catalytic process can be summarized in three main steps: (1) electron–hole generation within the MOF by means of solar-light absorption, (2) electron transfer to the co-catalyst and MOF recovery *via* sacrificial agent oxidation and (3) the catalytic reaction, for instance hydrogen (H_2) production. In this context, screening aiming at the detection of

[a]*Laboratory of Molecular Simulation, Institut des Sciences et Ingénierie Chimiques, Valais, Ecole Polytechnique Fédérale de Lausanne (EPFL), Rue de l'Industrie 17, CH-1951, Sion, Switzerland. E-mail: maria.fumanal@epfl.ch*

[b]*IBM Research Zurich, Säumerstrasse 4, 8803 Rüschlikon, Switzerland. E-mail: ita@ibm.zurich.ch*

[c]*Department of Mathematics, Vrije Universiteit Amsterdam, De Boelelaan 1111, 1081 HV Amsterdam, The Netherlands*

† Electronic supplementary information (ESI) available. See DOI: 10.1039/c9ta13506e

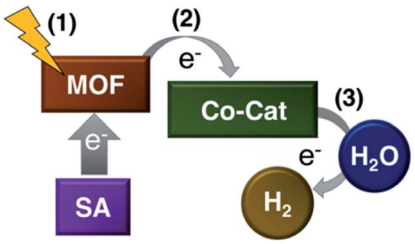

Fig. 1 Scheme of the photo-catalytic process including the MOF, co-catalyst (Co-Cat) and sacrificial agent (SA) for H_2 production.

photocatalytic MOFs must make a pragmatic differentiation between (i) the energetic requirements that a MOF must fulfil to potentially be a photocatalyst and (ii) the electronic features that will make it highly efficient in its catalytic purpose, that is, the electronic features that determine its performance and stability. The first step determines the actual UV-vis and redox capabilities of the MOF in a given photocatalytic system, while the second step analyzes desired properties for high efficiency, such as exciton lifetime and electron photoconductivity. This two-level distinction is important to first identify potentially photo-catalytically active MOFs by searching for their energetic requirements, and only then evaluate the performance of the identified materials in a second step. This strategy is motivated by the fact that long-lived electron–hole pairs and high electron mobility will only provide a photo-catalytic response in the presence of visible-light if both the absorption and the thermodynamic energy of the photoelectron are appropriate.

To evaluate the UV-vis capabilities of medium-large metal–organic complexes, low-energy absorption spectra calculations can be easily obtained from Density Functional Theory (DFT)[24–26] calculations and their Time-Dependent extension within the Linear-Response formalism (LR-TDDFT).[27–29] However LR-TDDFT calculations are rarely applied to MOF crystals[30] because their usually large size and cluster models are used instead.[31,32] As another simplification, the light absorption properties of periodic insulating or semiconducting systems have been traditionally associated with their electronic band gap. Nevertheless, it is still important to distinguish between the electronic band gap and the optical gap.[33] While the electronic band gap is associated with an excitation energy in which the electron–hole interaction is not taken into account, the optical gap describes the lowest neutral excitation of the system including excitonic effects. To anticipate the low-lying absorption energies of molecule-like systems such as MOFs, explicit calculations of excitation energies and optical spectra with excitonic features should be considered.[34] Unfortunately, these calculations are computationally expensive and cannot be applied in a high-throughput manner for periodic systems; thus estimations from the electronic band gap are required.

Similarly, the photo-reductive capabilities of a periodic system to produce H_2 can be estimated from the energy of its conduction band (CB), obtained with reference to the vacuum potential value. The latter is commonly obtained by means of artificially introducing a vacuum space in between bulk layers.[35] However, there are two problems that hinder the usage of this approach for MOFs: the lack of knowledge about the surface cut and the high computational cost of enlarging the unit cell of an already large porous material. To find a practical solution, Walsh and co-workers proposed to estimate the vacuum potential energy of porous MOFs from the value of the electrostatic potential energy at the centre of the largest pore of the framework,[36] thus providing a reference scale of the electronic levels. It is expected that the discovery of photo-catalytically active MOFs will highly benefit from high-throughput computations designed to screen these two target descriptors.

In this work, we propose a computational scheme to evaluate two energy-based property-descriptors of MOFs that are directly related to their ability to act as photocatalysts, and we apply it for a test-set of MOFs extracted from the Cambridge Structural Database (CSD).[37] The first descriptor assesses the UV-visible absorption capability and the second descriptor determines the photo-redox potential and MOF/co-catalyst band energy alignment, provided the electronic energy levels of the latter. Considering these two descriptors, our goal is to screen large databases of MOFs with cost-effective methods that are able to discriminate between promising candidates, rather than predicting accurate values. Analysing our test-set, we found that several of the systems for which we predict UV-vis absorption are confirmed to show UV-vis absorption experimentally. This supports the reliability of our procedure to identify promising candidates. In particular, one promising system for photo-catalytical water splitting was identified. Altogether, our procedure provides a cost-efficient method to screen large MOF databases in a high-throughput manner aiming to accelerate the discovery of MOF photocatalytic systems.

Methods

Dataset construction

Two datasets were constructed in this work from a CSD MOF subset reported in 2017.[37] The first dataset (labelled **DS1**) contains orthorhombic Zn MOFs with a unit cell volume up to 1000 Å^3, which results in 132 distinct crystalline structures. The CSD reference codes with the cell parameters and chemical composition are provided in Table S1 of the ESI.† The second dataset (**DS2**) contains porous Zn or Cd MOFs with a unit cell volume between 7000 and 8000 Å^3 and pore diameters between 5 and 13 Å as determined using the program Zeo++.[38] A complete list of the 73 parsed Zn and Cd MOFs is provided in Table S2 of the ESI† including the CSD reference codes, the cell parameters and the chemical composition. A distinction between the **DS1** and **DS2** datasets is made to assess the screening protocol for the UV-vis absorption and photo-redox properties, respectively, as explained below.

Computational details

Fix-cell geometry optimizations were initially performed for **DS1** and **DS2** crystal structures under periodic boundary conditions after a careful examination of the presence of disorder and/or the need for adding missing hydrogens. We did not consider

cell-parameters optimizations in our screening in order to reduce the computational cost and because we used experimentally reported values. However, cell-parameters optimization could be easily implemented in automated screening of MOF structures. The optimizations were performed using Quantum Espresso code[39] version 6.3. with the SSSP precision pseudopotential library.[40] The wave-function and charge-density cutoffs used are converged values with respect to phonon frequencies, pressure, cohesive energies and band structure calculations.[41] The PBE[42] functional with Grimme D3 dispersion[43] correction and a Γ-point sampling of the Brillouin zone was used. PBE single point calculations were performed on the optimized structures at two k-points equally spaced in each direction of the reciprocal lattice and until k-point sampling convergence.

A subset of the **DS1** optimized structures was further optimized using the PBE functional and Grimme D2 dispersion[44] correction at Γ with the CPMD package[45,46] version 4.1. Grimme D3 is not available in this version; however the use of D2 did not imply any significant change in the structure, and thus in the electronic properties. Troullier–Martins norm-conserving pseudopotentials[47] were used with a plane wave cutoff of 90 Ry for the orbitals and of 360 Ry for the density. Within the same setup, LR-TDDFT calculations were performed using periodic boundary conditions with the PBE and PBE0 (ref. 48 and 49) functionals for the **DS1** re-optimized structures. These calculations require a large computational cost that is not affordable for large systems such as the **DS2**. We randomly selected 20 structures of **DS2** to perform PBE0 energy calculations. For this subset, PBE0 ground state calculations were performed with the CP2K code version 5.1 (ref. 50) at the Γ k-point using the Goedecker–Teter–Hutter pseudopotentials[51] with a density cutoff of 450 Ry and the DZVP-MOLOPT basis set for non-metal atoms and the TZVP-MOLOPT basis set for Zn/Cd atoms.[52] The Auxiliary Density Matrix Method (ADMM) was used in order to reduce the computational cost together with the auxiliary basis set pFIT3 (3 Gaussian exponents per valence orbital, includes polarization d-functions) for non-metal atoms and cFIT11 (contracted, 4s, 3p, and 3d shells and 1f shell in total) for Zn/Cd atoms.

Electronic chemical potentials

Following the procedure previously reported by Walsh and coworkers,[36] the electrostatic potential average in the pore of the **DS2** optimized structures was obtained in place of the vacuum level. However, we found that the structural complexity of **DS2** MOFs makes the electrostatic potential at the geometrical centre of the pore an often inadequate choice for the electrostatic potential evaluation (Fig. S1 in the ESI†). This motivated us to implement an automated search for the point in the MOF pore with the smallest spatial variation of the electrostatic potential to most appropriately represent the reference energy level. The variances obtained were below 5×10^{-3} eV in all cases. This was included in a modified version of the already available MacroDensity package[53] (see Section S1 of the ESI†). Then, the Kohn–Sham energy levels ε_{KS} are aligned relative to this potential (Φ_{av}) as $\varepsilon_{KS}^{absolute} = \varepsilon_{KS} - \Phi_{av}$. The energy of the highest occupied level is taken as the ionization potential (IP). The electron affinity (EA) is calculated from the difference between the IP and the computed band gap E_g (EA = IP − E_g). Note that the IP/EA cannot be evaluated for the **DS1** structures because they lack a sizable pore to estimate the vacuum potential.

Results

The results are discussed in two main sections. In Section 1 we present the computational screening protocol to address a cost-effective evaluation of the UV-vis and photo-redox properties of the selected **DS1** and **DS2** MOFs. In Section 2, the outcomes of the test screening are presented. The MOFs that are predicted to be photoactive are discussed and the results for those of our systems that have been experimentally studied are validated by comparing them to the experimentally obtained results. Finally, the computed IP/EA map of **DS2** MOFs is used to predict band energy alignment synergies with respect to some prototype H_2O/H_2 co-catalysts.

Section 1. Screening procedure for UV-vis light absorption and redox properties of MOFs

The scheme to evaluate and predict the UV-visible absorption and photo-redox capabilities of MOF materials is shown in Fig. 2. In the following, we start by addressing the evaluation of the band gap and the lowest excitation energy with DFT methods.

Band gap. Electronic structure calculations of periodic crystals are easily accessible with DFT by applying Bloch's theorem to the Kohn–Sham equations.[54] Within periodic DFT, integration over the Brillouin zone (BZ) in reciprocal space is required, which is discretized in the so-called k-point mesh. An appropriate choice of the k-point sampling is crucial to obtain reliable results and needs to be carefully converged. The optimal number of k-points usually depends on the size of the unit cell, systematically decreasing for bigger unit cells. This is because the BZ decreases in the reciprocal space with increasing unit cell sizes. In this context, it is a common strategy to use

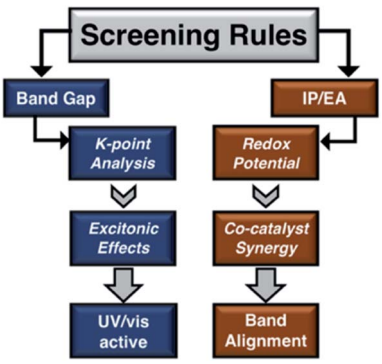

Fig. 2 Schematic protocol designed to evaluate UV-visible absorption capabilities and photo-oxidation (or photo-reduction) properties of a given material, herein applied for MOFs.

only one single k-point (called Γ) at the centre of the BZ for large supercells. This is usually the case for MOFs characterized with big pores and large unit cells, but still a statistical analysis for different sized data-sets has not been reported.

Γ-point and extended $2 \times 2 \times 2$ k-point sampling was used to evaluate the electronic band gap of **DS1** and **DS2** structures. The computed band gaps obtained for **DS1** range from 0.5 to 5 eV. The error at the Γ-point (ΔE_k) ranges from 0.0 to 2.0 eV and does not correlate with the band gap value (ΔE_k of $\sim$ 1 eV can be found in MOFs with a band gap of either 1.5 eV or 3.5 eV). The statistical analysis indicates that of the 132 cases, $\sim$20% show a correction of >0.25 eV, while $\sim$10% had a correction of more than 0.55 eV (Section S2 of the ESI†). Performing the same analysis on 45 selected **DS2** structures shows that the computed band gap ranges from 1.5 eV to 4.0 eV and ΔE_k is zero or negligible (<0.1 eV) in all cases. A small ΔE_k in the case of the **DS2** structures is ascribed to their large unit cell volumes (between 7000 and 8000 Å^3). In contrast, the relatively small volume of **DS1** (<1000 Å^3) results in significant errors in 20% of the cases. We performed an analysis of the dependence of ΔE_k on the unit cell volume and on the maximum ratio between the a, b, c unit cell parameters; however no direct correlations were found (see Section S2 in the ESI†). These examples show that a careful examination of the band gap convergence with respect to the k-point sampling is required for those particular cases that have small unit cells and large ratios between cell parameters. For LR-TDDFT calculations performed at Γ, we excluded the 28 **DS1** structures with ΔE_k > 0.25 eV. However, after assessing the protocol, those structures can be included by considering k-point converged band gap values. Converged values are given in Table S4 of the ESI.†

Excitation energies. As mentioned in the introduction, explicit calculations of excitation energies and optical spectra have to be considered to predict low-lying absorption energies. But since these calculations cannot be performed in a high-throughput manner on periodic systems given their high computational cost, estimations obtained from the electronic band gap are needed. It is known that the local density approximation (LDA) or generalized gradient approximation (GGA) functionals that are used for cost-effective calculations of electronic band gaps underestimate the electronic band gap of insulators and semiconductors systematically.[55] Consequently, large effort has been undertaken in order to compute accurate band gaps of solids from DFT band structure calculations.[56–58] Among different strategies such as GW perturbation theory[56] or Hubbard-corrected DFT+U,[59] hybrid schemes containing an admixture of nonlocal exact exchange have been shown to significantly improve the description of the electronic band gap for a variety of materials.[57,58] In the following, we aim at predicting the absorption properties of MOFs by establishing linear correlations between the generalized gradient approximation (GGA)-Perdew–Burke–Ernzerhof (PBE) and the hybrid-PBE0 functional. This allows us to correct the results obtained from the cheaper PBE band gap calculations to estimate the more accurate but more costly hybrid-PBE0 functional results. For that we performed calculations with both functionals for selected **DS1** structures including LR-TDDFT evaluations of their low-lying excited energies. The results obtained were then used to optimize linear correlation functions between the computed band gaps and the S_1 excited energies. The inclusion of exact exchange is crucial to properly address the electron–hole interaction of charge-transfer (CT) excited states. For this reason we use the hybrid PBE0 functional as the reference.[60]

We found that Γ-point sampling provides adequate estimations for 104 structures of the 132 **DS1** set. Of the 104 structures, 36 structures (35%) show a PBE band gap value below 3.2 eV, the energy associated with the upper limit of the visible light spectrum (380 nm). Given that GGA is well-known for underestimating band gaps, systems with higher values (band gap > 3.2 eV) were discarded as potential candidates for UV-vis absorption. Hence, PBE0 calculations were consequently performed for the remaining 36 systems to address the PBE–PBE0 correlations. The correlations obtained can then be applied for all cases in the context of screening.

To gain some insights into the excitonic effects, the low-lying excited state energies were computed at the PBE and PBE0 level using LR-TDDFT calculations with periodic boundary conditions. Correlations between the computed band gap and the lowest S_1 excited energies are shown in Fig. 3a and b, respectively. It can be seen that PBE TDDFT calculations do not account for excitonic effects, that is, the electronic band gap and the computed S_1 energy coincide. In contrast, the PBE0

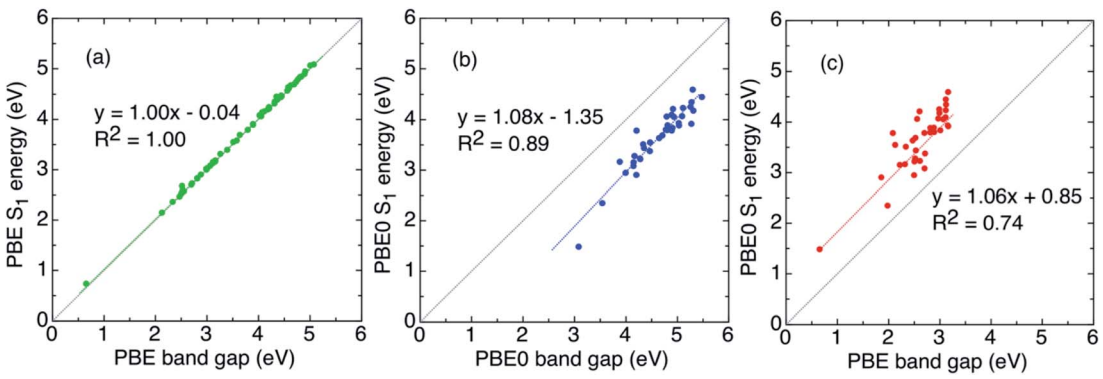

Fig. 3 Correlations between (a) the PBE band gap and PBE S_1 energy, (b) PBE0 band gap and PBE0 S_1 energy and (c) PBE band gap and PBE0 S_1 energy. Linear regression fittings are provided. Raw data is given in Table S6 of the ESI.†

results display a systematic reduction of about ~1.0 ± 0.5 eV from the band gap to the S_1 energy, which is ascribed to the exciton binding energy. The absence of excitonic effects in semilocal GGA–PBE functionals is due to the long-range behaviour not being correctly captured by the exchange kernel. Hybrid exchange functionals replace a portion of the semilocal exchange energy with the exact exchange energy, which in periodic insulators has the non-local behaviour necessary for the formation of excitons. However, the resulting unscreened electron–hole interaction may lead to an over-binding of the excitons.[33] The direct correlation between the PBE and PBE0 band gaps is shown in Fig. S5† and that between the PBE band gap and PBE0 S_1 energies is shown in Fig. 3c. Based on the root mean square value R^2 obtained from linear regression (0.74), one can anticipate that the prediction based on the band gaps will be subject to a significant error. A systematic shift of 0.85 eV will therefore be applied to the PBE gaps to estimate the lowest absorption edge.

Band energy alignment. While the electronic band gap of a given MOF determines whether it will absorb in the visible region, its redox properties are controlled by the absolute energies of its conduction and valence band-edges. These energies must be placed on an absolute scale within a band energy alignment diagram to consider their redox-capabilities with respect to a given reaction or their redox-synergy with a particular co-catalyst.[36,61–63] The valence and conduction band edges in solids can be represented by the energy of the highest occupied and lowest unoccupied energy levels, respectively, when aligned relative to a vacuum reference potential. After this alignment, they can be associated with the ionization potential (IP) and electron affinity (EA) of the material, respectively, the difference of which corresponds to the electronic band gap (see the Methods).

So far, our previous evaluation of the electronic band gap did not provide information about the position of the band-edges and thus cannot be used to predict any photo-catalytic activity. To this aim, we computed the electrostatic potential at a representative point inside the largest pore of the **DS2** structures (see the Methods and Fig. S1 of the ESI†) and used this value as the vacuum potential.[36] The IP and EA were then obtained from the highest occupied and lowest unoccupied absolute energy levels as explained above. The PBE and PBE0 results obtained for 20 selected **DS2** structures are represented in Fig. 4 (raw data are given in Table S8 of the ESI†). Remarkably, this shows that the predicted redox-capabilities can strongly depend on the level of theory used (PBE or PBE0) and thus accurate references are needed.

Linear regressions between the PBE and PBE0 computed IP and EA values were optimized in order to establish empirical rules to estimate the valence and conduction band-edges, respectively. The correlations obtained (Fig. 5) provide R^2 values above 0.9 and predict an average shift of −0.7 eV between the PBE and PBE0 computed IP and of +0.9 eV in the case of EA. The negative and positive shifts of the IP and EA values, respectively, that appear when exact exchange is included, are in agreement with the expected opening of the underestimated PBE band gap. However, it is worth emphasizing that the correction does not equally apply to the valence and conduction bands, being systematically larger for the latter. Applying the proposed shifts to the PBE values results in a mean absolute error below 0.1 eV with respect to the PBE0 calculations.

The resulting computational protocol to evaluate the potential of MOFs as photocatalysts can now be applied for all systems, summarized in the following steps:

(1) Geometry optimization of the MOF structure and calculation of the band gap converged in the reciprocal space at the PBE level.

(2) Estimation of the light-absorption edge by shifting the PBE band gap by +0.85 eV. Discard those systems with a corrected band gap above 3.2 eV.

(3) For porous MOFs, evaluation of the vacuum electrostatic potential at the MOF pore and shifting of the VB and CB energies computed at the PBE level by −0.7 and +0.9 eV, respectively.

(4) Building a band energy diagram between the screened MOFs and the co-catalyst or reaction of interest to assess if

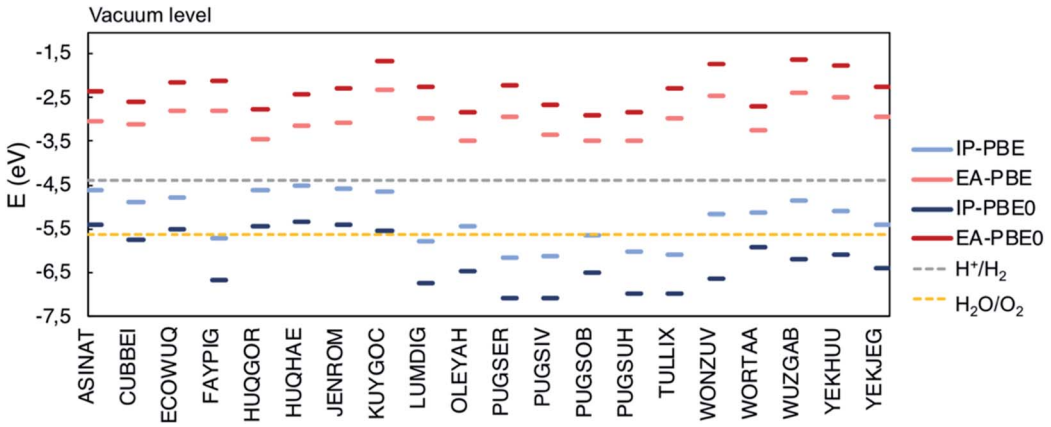

Fig. 4 Computed ionization potential (blue) and electron affinity (red) of 20 selected **DS2** structures with respect to the vacuum level which is chosen as the electrostatic potential inside the pore of the MOF. PBE and PBE0 values are provided, as well as the reference H^+/H_2 and H_2O/O_2 potentials. Raw data are collected in Table S8 of the ESI.†

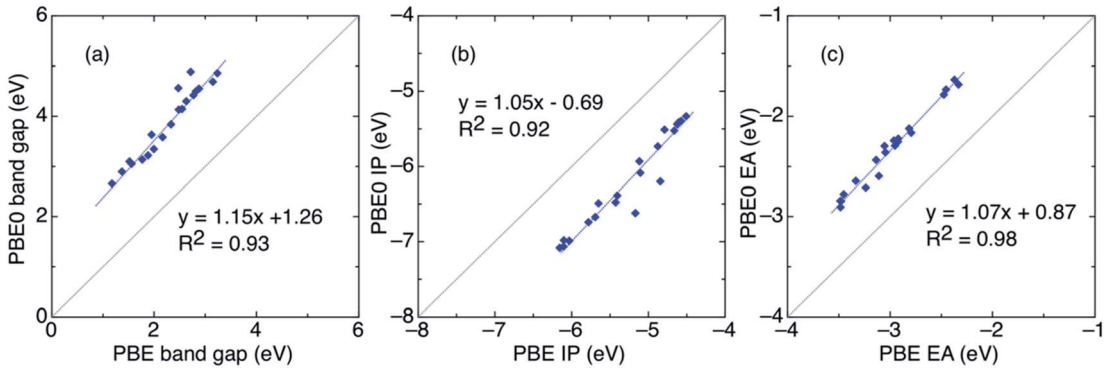

Fig. 5 Correlation between the PBE and PBE0 obtained values of the (a) band gap, (b) ionization potential IP and (c) electron affinity EA of the 20 selected **DS2** structures. Linear regression fittings are provided. The IP and EA values correspond to the highest occupied and lowest unoccupied energy levels. Raw data are collected in Table S8 of the ESI.†

electron/hole injection will be favourable. For instance, for H^+/H_2 production discard those systems with a CB below −4.4 eV.

Section 2. Screening of the UV-vis absorption, IP/EA map and co-catalyst band alignment

In this section, we discuss the computational screening of all the MOFs in the sets **DS1** and **DS2** by applying the screening protocol developed in the previous section.

On the basis of the estimated optical band gaps, we find that 11 **DS1** structures potentially absorb below 3.5 eV. Relevant information about these materials is collected in Table 1, including their CSD reference codes and their main chemical compositions. Out of the 11 systems, 6 are hybrid inorganic–organic nanostructures consisting of ZnSe or ZnTe layers that are connected by diamine molecules as spacers. Notably, these composite materials were designed with the aim of combining the semiconducting functionality of the inorganic constituent with the low weight and high processability of the organic component. In particular, they offer significant variations in the optical properties of their inorganic frameworks and provide considerably blue-shifted absorption-edges starting at 3.3 eV in the case of ZnTe composites[64] and at 3.9 eV in the case of ZnSe.[68] Our estimated values overstabilize their lowest absorption edge by ∼0.6 eV, while predicting the correct trend between the two sets of ZnTe and ZnSe compounds. Similarly, photoluminescence studies were undertaken on material **2** from Table 1, for which a moderately blue-green fluorescence was measured upon excitation at 325 nm.[65] This system contains a well-known photoactive azobenzene group characterized by two relatively intense bands in the UV spectrum at 220–240 and 320–360 nm and weak absorption in the visible region >400 nm,[82] in agreement with our estimation. The optical properties of the other 4 screened compounds were not reported in their original publications. However, naphthalene compounds, such as **9** and **11** in Table 1, are well known for their widespread application in the fluorescence field, being characterized by an absorption band-edge at ∼350 nm,[83] and indole derivatives are characterized by optical absorption spectra starting above 300 nm, as has been predicted for system **6**.[84]

Despite the large diversity of the chemical composition of the studied materials, our screening based on PBE calculations corrected from PBE0 S_1 energies was able to identify a set of systems for which low-energy absorption is experimentally expected. Remarkably, it is found that their characteristic UV-vis absorption bands can either originate in the ZnTe/ZnSe

Table 1 The 11 MOFs from **DS1** that potentially absorb below 3.5 eV, with their computed (PBE0) and predicted (PBE-corrected: PBE-c) UV-vis absorption energies (eV) and wavelengths (nm). PBE-c is obtained by adding 0.85 eV to the PBE band gap. The PBE0 S_1 energies are the reference values. The CSD reference codes and the chemical composition in terms of the metal cluster and the main ligand are also given

	CSD ref.	PBE-c (eV)	PBE0 S1 (eV)	Abs. diff (eV)	Abs-c (nm)	Abs PBE0 (eV)	Metal cluster	Main ligand
1	QOBHEU[64]	2.828	2.349	0.479	439	528	ZnTe	Ethylenediamine
2	QENFUL[65]	2.705	2.905	−0.200	458	427	ZnO_4N_2	Pyridyl-diaza-butadiene
3	QOBHEU01 (ref. 64)	3.345	2.948	0.397	371	421	ZnTe	Ethylenediamine
4	QOBHIY[64]	3.549	3.082	0.467	349	402	ZnTe	Propanediamine
5	PYZNDT[66]	3.067	3.152	−0.085	404	393	ZnO_4N_1	Pyridine-dithionate
6	PUBGID[67]	3.167	3.165	0.002	391	392	ZnO_6	Indole-carboxylate
7	MICDUX[68]	3.352	3.219	0.133	370	385	ZnSe	Ethylenediamine
8	VAMWEM[69]	3.458	3.230	0.228	359	384	ZnSe	Butanediamine
9	IYEXEP[70]	3.366	3.279	0.087	368	378	ZnO_4	Naphthalene-dicarboxylate
10	MICFAF[68]	3.559	3.377	0.182	348	367	ZnSe	Propylenediamine
11	HERYOT[71]	3.379	3.438	−0.059	367	361	ZnO_6	Naphthalene-tetracarboxylate

inorganic layers or are localized in optically active ligands such as azobenzene/naphthalene. This highlights the complexity of assessing empirical models to accurately predict their optical band gap and points to the need for *ab initio* calculations. However, we demonstrated that reasonable estimations can be made from cost-effective methods such as PBE by establishing direct correlations with accurate methods, such as the hybrid PBE0 used herein. Future high-throughput screenings applied on MOFs are envisioned with this purpose.

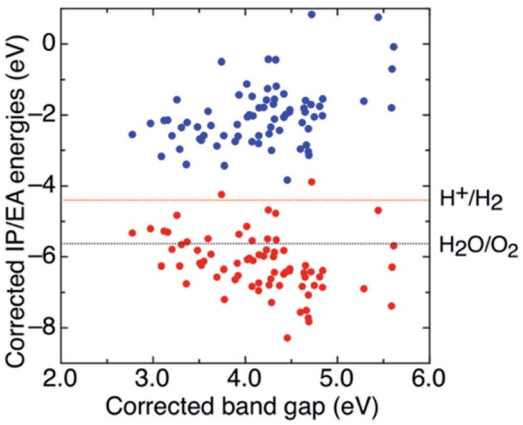

Fig. 6 PBE-corrected IP (red) and EA (blue) energies of the **DS2** structures mapped to their PBE-corrected band gap values (data in Table S9 of the ESI†).

PBE-corrected IP and EA values for all the **DS2** structures are plotted in Fig. 6 along with their corresponding electronic band gaps. The computed EA values indicate that all systems will be energetically able to reduce H^+/H_2 upon excitation. This can be inferred from the conduction band edge being located above the H^+/H_2 redox potential in all cases. In contrast, the position of the valence band edge is found either above or below the redox potential that is needed to generate O_2. Only in the cases in which the EA and IP are predicted to be above the H^+/H_2 and below the H_2O/O_2 redox potentials, the system is potentially capable of cleaving water upon absorption of light.[85] If the valence band edge is above the H_2O/O_2 redox potential, a sacrificial agent becomes necessary to recover the neutral MOF provided that their redox-synergy is appropriate.

The IP and EA corrected energies are spread over ~4.5 eV ranging from −4.0 to 0.5 eV for the EA and from −4.0 to −8.5 eV for the IP. In the following, we restrict our consideration to those structures whose corrected band gaps predict light absorption in the visible spectrum. This decision was made with the same screening procedure that is outlined above for **DS1**. We tentatively consider a band gap energy threshold of 0.2 eV above the upper limit of the visible spectrum (3.2 eV) in order to ensure that potential candidates are not discarded due to the estimation error committed. Among the 73 explored structures, 11 (15%) are identified as potentially absorbing in the visible range of light since they have corrected band gaps below 3.4 eV. Relevant information about the screened materials is collected in Table 2, including the CSD reference codes

Table 2 The 11 MOFs from **DS2** that potentially absorb below 3.4 eV, with their computed PBE and PBE-corrected IP and EA values (eV). PBE-corrected band gaps obtained as EA−IP are also given. The CSD reference codes and the chemical composition considering the constituent ligands are provided

	CSD ref	PBE IP (eV)	PBE EA (eV)	Band gap (eV)	IP − 0.7 (eV)	EA + 0.9 (eV)	Main ligands
1	HUQGOR[72]	−4.627	−3.453	2.774	−5.327	−2.553	Nitrilotribiphenyl-4-carboxylate Ethene-1,2-diyldipyridine
2	HUQHAE[72]	−4.508	−3.137	2.971	−5.208	−2.237	Nitrilotribiphenyl-4-carboxylate Ethene-1,2-diyldipyridine
3[a]	DEVWOT[73]	−5.559	−4.070	3.089	−6.259	−3.170	1,2-Bis(4,4′-bipyridinium)ethane 5-methylisophthalate
4	JENROM[74]	−4.574	−3.055	3.119	−5.274	−2.155	Nitrilotribiphenyl-4-carboxylate 4,4′-Bipyridine
5	ASINAT[75]	−4.604	−3.046	3.158	−5.304	−2.146	Nitrilotribiphenyl-4-carboxylate Di(pyridin-4-yl)-4*H*-1,2,4-triazol-4-amine
6	WARFAZ[76]	−5.091	−3.486	3.205	−5.791	−2.586	L-Alanine naphthalene diimide 4,4′-Bipyridine
7[b]	ZUCGAH[77]	−4.127	−2.468	3.258	−4.827	−1.568	Benzyl substituted porphyrin
8	MUQSAU[78]	−5.557	−3.868	3.288	−6.257	−2.968	Biphenyl-2,2′,6,6′-tetracarboxylate Ethene-1,2-diyldipyridine
9[c]	XEJJII[79]	−4.959	−3.253	3.307	−5.659	−2.353	Furan-2,5-dicarboxylate (Selenophene-2,5-diyl)dipyridine
10	VULWEF[80]	−6.055	−4.295	3.360	−6.755	−3.395	Benzene-1,4-dicarboxylate (4-Carboxyphenyl)-4,4′-bipyridinium
11[d]	CUBBEI[81]	−4.878	−3.110	3.368	−5.578	−2.210	Curcumin

[a] Absorption in the visible has been reported for system 3 associated to a charge-transfer transition. [b] System 7 corresponds to the porphyrin precursor used to synthesise a photo-redox catalyst including boron-dipyrromethene. [c] UV-vis absorption of 9 is associated to local π–π* transitions of the aromatic rings in the framework. [d] Curcumin is a yellow pigment characterised by an π–π* electronic transition that becomes blue-shifted upon metal-complexation.

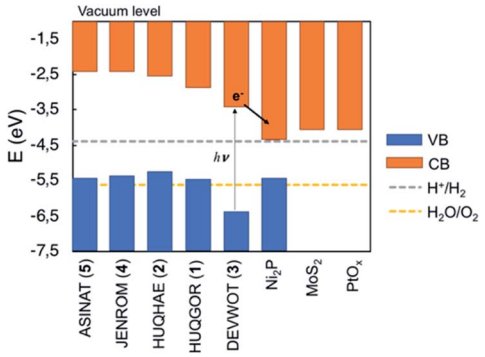

Fig. 7 Diagram of the electronic energy levels computed in this work for selected DS2 MOFs and values collected for representative co-catalysts.[10,86,87]

and main chemical compositions. The systems cover a wide range of properties from single-crystal transmetalation reactions reported for **1**, **2**, **4** and **5**,[72,74,75] to selective CO_2 capture for **8**.[78] Notably, UV-visible absorption has been experimentally reported for systems **3**,[73] **7**,[77] **9** (ref. 79) and **11** (ref. 81) associated with charge-transfer or local π–π* excitations within the ligands. The fact that the screening predicts UV-vis absorption capabilities for these systems supports the reliability of the cost-effective approximations performed.

From the energies of the valence- and conduction-band edges of the systems, energy–band diagrams for the different components of the catalytic complex can be constructed. These allows anticipating the direction of the photoinduced electron injection. One possible strategy is to combine photoactive MOFs with appropriate co-catalysts to boost the photocatalytic performance. For photocatalytic hydrogen (H_2) production, representative examples of reduction co-catalysts that promote proton reduction in conjunction with MOFs are Ni_2P,[10] Pt[86] or MoS_2 (ref. 87) nanoparticles. The band alignment synergies of these co-catalysts with the first five **DS2** MOFs from Table 2 are shown in Fig. 7. Particularly promising is compound **3** (DEVWOT)[72] for which both the UV-vis and photo-redox requirements for the water splitting photocatalytic purpose are fulfilled. This MOF was specifically designed to display low-energy charge transfer (CT) phenomena by means of π-stacking interactions between electron-rich and electron-deficient units. In particular, UV-vis light excitation promotes CT from the phenyl-carboxylate to bipyridine components (see Fig. 8). The non-local character of the excitation could even improve the photocatalytic activity as it is associated with long exciton lifetimes.

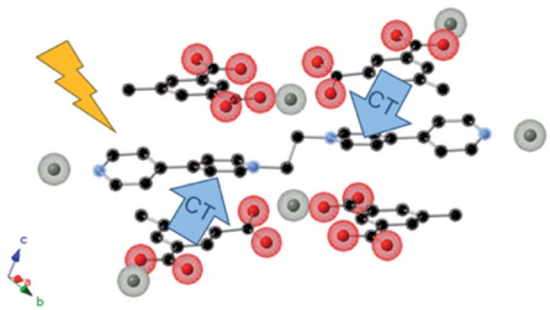

Fig. 8 Schematic representation of photoinduced charge transfer (CT) between donor and acceptor units in MOF **3** of DS2 (DEVWOT).[73] Colour code: oxygen in red, nitrogen in blue, carbon in black, and Zn in grey. Hydrogens are omitted for clarity.

Conclusions

With the rapid increase of available crystallographic data of MOFs, the use of high-throughput computational screening has become a promising tool to aid the identification and characterization of materials with desired properties. Although any computationally accessible descriptor can be in principle included in a high-throughput screening process, its rapidness and feasibility are still requirements for a screening to become an efficient and valuable complementary approach to the experiments. This makes the design of cost-effective property-descriptors essential, as well as the determination of the error committed and its validation.

In this work, we propose a screening protocol to evaluate two energy-based descriptors that are directly related to the performance of MOFs as photocatalysts. These descriptors assess the UV-vis absorption capabilities and photo-redox properties based on DFT electronic structure calculations. Our results show that the first can be directly estimated from the PBE band gap considering a systematic shift of 0.85 eV that corrects the well-known overestimation of GGA functionals, as well as the inability of PBE to account for excitonic effects in solids. Furthermore, the absolute position of the conduction- and valence-bands is evaluated with respect to the electrostatic potential computed at a representative point inside the pore of the MOF structure, which is taken as the vacuum potential. Comparing PBE and PBE0 calculations shows a systematic shift of −0.7 for the valence band and of +0.9 eV for the conduction band.

Performing the screening on all the structures of our selected test-sets of MOFs allowed us to validate the strategy and provided a set of photoactive MOFs that have been synthesised but not studied with respect to their photo-catalytic activity. In particular, MOF structure **3** of **DS2** (DEVWOT) displays suitable UV-vis light absorption and desirable absolute VB and CB energies for water splitting, as well as promising excited state features for long lived excitonic lifetimes. Future analysis is envisioned to include these and other performance descriptors associated with enhanced photo-catalytic activity.

Conflicts of interest

There are no conflicts to declare.

Acknowledgements

This work was supported by the EPFL and the National Centre of Competence in Research (NCCR) Materials' Revolution: Computational Design and Discovery of Novel Materials

(MARVEL) of the Swiss National Science Foundation (SNSF). Calculations were performed at the EPFL High Performance Computing Center SCITAS. All the dataset files are available on the Materials Cloud Archive at https://archive.materialscloud.org/.

Notes and references

1 G. Ferey, *Chem. Soc. Rev.*, 2008, **37**, 191–214.
2 J. A. Mason, J. Oktawiec, M. K. Taylor, M. R. Hudson, J. Rodriguez, J. E. Bachman, M. I. Gonzalez, A. Cervellino, A. Guagliardi, C. M. Brown, P. L. Llewellyn and N. Masciocchi, *Nature*, 2015, **527**, 357–361.
3 J.-R. Li, R. J. Kuppler and H.-C. Zhou, *Chem. Soc. Rev.*, 2009, **38**, 1477–1504.
4 J. Liu, L. Chen, H. Cui, J. Zhang, L. Zhang and C.-Y. Su, *Chem. Soc. Rev.*, 2014, **43**, 6011–6061.
5 A. Corma, H. García and F. X. Llabreś i Xamena, *Chem. Rev.*, 2010, **110**, 4606–4655.
6 W. P. Lustig, S. Mukherjee, N. D. Rudd, A. V. Desai, J. Li and S. K. Ghosh, *Chem. Soc. Rev.*, 2017, **46**, 3242–3285.
7 H.-C. Zhou, J. R. Long and O. M. Yaghi, *Chem. Rev.*, 2012, **112**, 673–674.
8 A. Schoedel, M. Li, D. Li, M. O'Keeffe and O. M. Yaghi, *Chem. Rev.*, 2016, **116**, 12466–12535.
9 B. Valizadeh, T. N. Nguyen and K. C. Stylianou, *Polyhedron*, 2018, **145**, 1–15.
10 S. Kampouri, T. N. Nguyen, C. P. Ireland, B. Valizadeh, F. M. Ebrahim, G. Capano, D. Ongari, A. Mace, N. Guijarro, K. Sivula, A. Sienkiewicz, L. Forró, B. Smit and K. C. Stylianou, *J. Mater. Chem. A*, 2018, **6**, 2476–2481.
11 S. Kampouri, T. N. Nguyen, M. Spodaryk, R. G. Palgrave, A. Züttel, B. Smit and K. C. Stylianou, *Adv. Funct. Mater.*, 2018, **28**, 1806368.
12 A. Dhakshinamoorthy, Z. Li and H. Garcia, *Chem. Soc. Rev.*, 2018, **47**, 8134–8172.
13 L. Chen, Y. Wang, F. Yu, X. Shen and C. Duan, *J. Mater. Chem. A*, 2019, **7**, 11355–11361.
14 M. A. Syzgantseva, C. P. Ireland, F. M. Ebrahim, B. Smit and O. A. Syzgantseva, *J. Am. Chem. Soc.*, 2019, **141**, 6271–6278.
15 S. Yuan, J.-S. Qin, H.-Q. Xu, J. Su, D. Rossi, Y. Chen, L. Zhang, C. Lollar, Q. Wang, H.-L. Jiang, D. H. Son, H. Xu, Z. Huang, X. Zou and H.-C. Zhou, *ACS Cent. Sci.*, 2018, **4**, 105–111.
16 C. Li, H. Xu, J. Gao, W. Du, L. Shangguan, X. Zhang, R.-B. Lin, H. Wu, W. Zhou, X. Liu, J. Yao and B. Chen, *J. Mater. Chem. A*, 2019, **7**, 11928–11933.
17 C. E. Wilmer, M. Leaf, C. Y. Lee, O. K. Farha, B. G. Hauser, J. T. Hupp and R. Q. Snurr, *Nat. Chem.*, 2012, **4**, 83–89.
18 M. C. Bernini, D. Fairen-Jimenez, M. Pasinetti, A. J. Ramirez-Pastor and R. Q. Snurr, *J. Mater. Chem. B*, 2014, **2**, 766–774.
19 C. M. Simon, J. Kim, D. A. Gomez-Gualdron, J. S. Camp, Y. G. Chung, R. L. Martin, R. Mercado, M. Deem, D. Gunter, M. Haranczyk and D. S. Sholl, *Energy Environ. Sci.*, 2015, **8**, 1190–1199.
20 Y. J. Colon, D. Fairen-Jimenez, C. E. Wilmer and R. Q. Snurr, *J. Phys. Chem. C*, 2014, **118**, 5383–5389.
21 S. Li, Y. G. Chung and R. Q. Snurr, *Langmuir*, 2016, **32**(40), 10368–10376.
22 G. Avci, S. Velioglu and S. Keskin, *ACS Appl. Mater. Interfaces*, 2018, **10**, 33693–33706.
23 A. S. Rosen, J. M. Notestein and R. Q. Snurr, *J. Comput. Chem.*, 2019, **40**, 1305–1318.
24 P. P. Hohenberg and W. Kohn, *Phys. Rev.*, 1964, **136**, B864.
25 W. Kohn and L. Sham, *Phys. Rev.*, 1965, **140**, A1133.
26 D. J. Becke, *Chem. Phys.*, 1993, **98**, 5648.
27 E. Runge and E. K. U. Gross, *Phys. Rev. Lett.*, 1984, **52**, 997.
28 M. Petersilka, U. J. Grossmann and E. K. U. Gross, *Phys. Rev. Lett.*, 1996, **76**, 1212.
29 M. E. Casida and M. Huix-Rotlant, *Annu. Rev. Phys. Chem.*, 2012, **63**, 287–323.
30 I. I. Vrubel, N. Y. Senkevich, E. V. Khramenkova, R. G. Polozkov and I. A. Shelykh, *Adv. Theory Simul.*, 2018, **1**, 1800049.
31 M. Ji, X. Lan, Z. Han, C. Hao and J. Qiu, *Inorg. Chem.*, 2012, **51**(22), 12389–12394.
32 L. Wilbraham, F.-X. Coudert and I. Ciofini, *Phys. Chem. Chem. Phys.*, 2016, **18**, 25176–25182.
33 A. C. Ullrich and Z.-h. Yang, *Top. Curr. Chem.*, 2016, **368**, 185–218.
34 J. Wiktor, I. Reshetnyak, M. Strach, M. Scarongella, R. Buonsanti and A. Pasquarello, *J. Phys. Chem. Lett.*, 2018, **9**, 5698–5703.
35 M. V. Mamonova and V. V. Prudnikov, *Russ. Phys. J.*, 1998, **41**(12), 1174–1179.
36 K. T. Butler, C. H. Hendon and A. Walsh, *J. Am. Chem. Soc.*, 2014, **136**, 2703–2706.
37 P. Z. Moghadam, A. Li, A. B. Wiggin, A. Tao, A. G. P. Maloney, P. A. Wood, S. C. Ward and D. Fairen-Jimenez, *Chem. Mater.*, 2017, **29**, 2618–2625.
38 T. F. Willems, C. H. Rycroft, M. Kazi, J. C. Meza and M. Haranczyk, *Microporous Mesoporous Mater.*, 2012, **149**, 134–141.
39 P. Giannozzi, *et al.*, *J. Phys.: Condens. Matter*, 2009, **21**, 395502.
40 G. Prandini, A. Marrazzo, I. E. Castelli, N. Mounet and N. Marzari, *npj Comput. Mater.*, 2018, **4**, 72.
41 *Standard solid-state pseudopotentials (SSSP)*, http://www.materialscloud.org/sssp/.
42 J. P. Perdew, K. Burke and M. Ernzerhof, *Phys. Rev. Lett.*, 1996, **77**, 3865.
43 S. Grimme, J. Antony, S. Ehrlich and H. Krieg, *J. Chem. Phys.*, 2010, **132**, 154104.
44 S. Grimme, *J. Comput. Chem.*, 2006, **27**, 1787–1799.
45 D. Marx and J. Hutter, *Mod. Methods Algorithms Quantum Chemistry, NIC*, ed. J. Grotendorst, Forschungszentrum Jülich, 2000, ch. 13, pp. 301–449.
46 W. Andreoni and A. Curioni, *Parallel Comput.*, 2000, **26**, 819–842.
47 N. Troullier and J. L. Martins, *Phys. Rev. B: Condens. Matter Mater. Phys.*, 1991, **43**, 1993.
48 M. Ernzerhof and G. E. Scuseria, *J. Chem. Phys.*, 1999, **110**, 5029–5036.

49 C. Adamo and V. Barone, *J. Chem. Phys.*, 1999, **110**, 6158–6169.
50 J. Hutter, M. Iannuzzi, F. Schiffmann and J. VandeVondele, *Wiley Interdiscip. Rev.: Comput. Mol. Sci.*, 2014, **4**, 15–25.
51 S. Goedecker, M. Teter and J. Hutter, *Phys. Rev. B: Condens. Matter Mater. Phys.*, 1996, **54**, 1703.
52 J. VandeVondele and J. Hutter, *J. Chem. Phys.*, 2007, **127**, 114105.
53 https://github.com/WMD-group/MacroDensity.
54 P. Kratzer and J. Neugebauer, *Front. Chem.*, 2019, **7**, 106.
55 M. K. Y. Chan and G. Ceder, *Phys. Rev. Lett.*, 2010, **105**, 196403.
56 A. Morales-García, R. Valero and F. Illas, *J. Phys. Chem. C*, 2017, **121**, 18862–18866.
57 J. Muscat, A. Wander and N. M. Harrison, *Chem. Phys. Lett.*, 2001, **34**(21), 397–401.
58 J. P. Perdew, W. Yang, K. Burke, Z. Yang, E. K. U. Gross, M. Scheffler, G. E. Scuseria, T. M. Henderson, I. Y. Zhang, A. Ruzsinszky, H. Peng, J. Sun, E. Trushin and A. Görling, *Proc. Natl. Acad. Sci. U. S. A.*, 2017, **114**, 2801–2806.
59 B. Himmetoglu, A. Floris, S. de Gironcoli and M. Cococcioni, *Int. J. Quantum Chem.*, 2014, **114**, 14–49.
60 A. Drew and M. Head-Gordon, *J. Am. Chem. Soc.*, 2004, **126**(12), 4007–4016.
61 A. Walsh and K. T. Butler, *Acc. Chem. Res.*, 2014, **472**, 364–372.
62 A. Walsh, K. T. Butler and C. H. Hendon, *MRS Bull.*, 2016, **41**(11), 870–876.
63 J. Calbo, M. J. Golomb and A. Walsh, *J. Mater. Chem. A*, 2019, **7**, 16571.
64 X. Huang and J. Li, *J. Am. Chem. Soc.*, 2000, **122**, 8789–8790.
65 G. Zhang, G. Yang and J. S. Ma, *Cryst. Growth Des.*, 2006, **6**, 1897–1902.
66 C. T. Kiers and A. Vos, *Acta Crystallogr., Sect. B: Struct. Crystallogr. Cryst. Chem.*, 1978, **34**, 1499–1504.
67 B. Morzyk-Ociepa, *Vib. Spectrosc.*, 2009, **49**, 68–79.
68 X. Huang, H. R. Heulings IV, V. Le and J. Li, *Chem. Mater.*, 2001, **13**, 3754–3759.
69 X. Huang and J. Li, *Mater. Res. Soc. Symp. Proc.*, 2002, **728**, 17–22.
70 K. O. Kongshaug and H. J. Fjellva, *Solid State Chem.*, 2004, **177**, 1852–1857.
71 R. K. B. Nielsen, K. O. Kongshaug and H. Fjellvåg, *Solid State Sci.*, 2006, **8**, 1237–1242.
72 D. De, S. Neogi, E. C. Sañudo and P. K. Bharadwaj, *Chem. - Eur. J.*, 2015, **21**, 17422.
73 X.-D. Yang, R. Zhu, L. Sun, R.-Y. Guo and J. Zhang, *Inorg. Chem.*, 2018, **57**(5), 2724–2729.
74 M. Qinghua, *CSD Communication*, 2017.
75 D. De, S. Neogi and P. K. Bharadwaj, *Cryst. Growth Des.*, 2016, **16**(9), 5238–5246.
76 S. A. Boer and D. R. Turner, *CrystEngComm*, 2017, **19**, 2402.
77 A. M. Lifschitz, R. M. Young, J. Mendez-Arroyo, C. L. Stern, C. M. McGuirk, M. R. Wasielewski and C. A. Mirkin, *Nat. Commun.*, 2015, **6**, 6541.
78 Y.-L. Xu, Q. Gao, M. Zhao, H.-J. Zhang, Y.-H. Zhang and Z. Chang, *Chin. Chem. Lett.*, 2017, **28**, 55–59.
79 C. Hua and D. M. D'Alessandro, *Cryst. Growth Des.*, 2017, **17**, 6262–6272.
80 M. Higuchi, D. Tanaka, S. Horike, H. Sakamoto, K. Nakamura, Y. Takashima, Y. Hijikata, N. Yanai, J. Kim, K. Kato, Y. Kubota, M. Takata and S. Kitagawa, *J. Am. Chem. Soc.*, 2009, **131**, 10336–10337.
81 H. Su, F. Sun, J. Jia, H. He, A. Wang and G. Zhu, *Chem. Commun.*, 2015, **51**, 5774.
82 P. H. Goreowen and H. Wheeler, *J. Org. Chem.*, 1961, **269**, 3295–3298.
83 I. P. Bincy, T. Srinivasan, S. N. Jaisankar and V. Ramkumar, *Solid State Sci.*, 2019, **89**, 85–92.
84 C. Lo, B. I. Doucoure, J.-J. Aaron, J. Svoboda, V. Kozmik, J.-C. Brochon, E. Henry, F. Maurel and M. Capochichi, *Spectrochim. Acta, Part A*, 2014, **120**, 47–54.
85 M. Grätzel, *Nature*, 2001, **414**, 338–344.
86 Y. Horiuchi, T. Toyao, M. Saito, K. Mochizuki, M. Iwata, H. Higashimura, M. Anpo and M. Matsuoka, *J. Phys. Chem. C*, 2012, **116**, 20848–20853.
87 T. N. Nguyen, S. Kampouri, B. Valizadeh, W. Luo, D. Ongari, O. M. Planes, A. Züttel, B. Smit and K. C. Stylianou, *ACS Appl. Mater. Interfaces*, 2018, **10**, 30035–30039.

